DTU Library

Dual-polarization NFDM transmission with continuous and discrete spectral modulation

Da Ros, Francesco; Civelli, Stella; Gaiarin, Simone; Porto da Silva, Edson; De Renzis, Nicola; Secondini, Marco; Zibar, Darko

Dual-polarization NFDM transmission with continuous and discrete spectral modulation

F. Da Ros, S. Civelli, S. Gaiarin, E.P. da Silva, N. De Renzis, M. Secondini, and D. Zibar

Abstract—Nonlinear distortion experienced by signals during their propagation through optical fibers strongly limits the throughput of optical communication systems. Recently, a strong research focus has been dedicated to nonlinearity mitigation and compensation techniques. At the same time, a more disruptive approach, the nonlinear Fourier transform (NFT), aims at designing signaling schemes more suited to the nonlinear fiber channel. In a short period, impressive results have been reported by modulating either the continuous spectrum or the discrete spectrum. Additionally, very recent works further introduced the opportunity to modulate both spectra for single polarization transmission. Here, we extend the joint modulation scheme to dual-polarization transmission by introducing the framework to construct a dual-polarization optical signal with the desired continuous and discrete spectra. After a brief analysis of the numerical algorithms used to implement the proposed scheme, the first experimental demonstration of dual-polarization joint nonlinear frequency division multiplexing (NFDM) modulation is reported for up to 3200 km of low-loss transmission fiber. The proposed dual-polarization joint modulation schemes enables to exploit all the degrees of freedom for modulation (both polarizations and both spectra) provided by a single-mode fiber (SMF).

Index Terms—nonlinear frequency division multiplexing, Raman amplification, nonlinear Fourier transform, inverse scattering transform

I. Introduction

OPTICAL communication systems have experienced an impressive growth over the past few decades with ever increasing transmission rates. Such a growth has been the results of key enabling technologies that have allowed to counteract the several physical effects hindering the transmission. As linear effects such as loss and dispersion can be dealt with in the telecommunication C-band, one of the current limiting factor preventing to further enhance the throughput of SMFs is the impact of Kerr nonlinearity. Whereas a significant research effort has been devoted to counteract nonlinear distortion experienced by the

Manuscript received October 18th, 2018;

F. Da Ros, S. Gaiarin, N. De Renzis, and D. Zibar are with the Department of Photonics Engineering, Technical University of Denmark, Kongens Lyngby, 2800 Denmark, e-mail: {fdro,simga,nidre,dazi}@fotonik.dtu.dk

S. Civelli and M. Secondini are with the TeCIP Institute, Scuola Superiore Sant'Anna, Pisa, Italy, email: {stella.civelli,marco.secondini}@santannapisa.it

E.P. da Silva was with the Department of Photonics Engineering, Technical University of Denmark, Kongens Lyngby, 2800 Denmark. He is now with the Department of Electrical Engineering of the Federal University of Campina Grande (UFCG), Paraba, Brazil, email:edson.silva@dee.ufcg.edu.br.

F. Da Ros, S. Civelli and S. Gaiarin equally contributed to this work.

signals during propagation, with solutions presented both in the optical and digital domain [1], no clear practical solution has yet been devised. Over the past few years, a theoretical approach, which had led to soliton-based communication, has been rediscovered [2], [3]. Soliton-based communication was developed in the 1980's [4]–[6], and, in particular, eigenvalue based communication was first attempted in [7], before the advent of wavelength-division multiplexing (WDM), and it was quickly abandoned due to its low spectral efficiency, challenges with fiber loss, noise and soliton-soliton interaction and the lack of coherent transceivers enabling access to the full electrical field. Recently, however, a generalization of the mathematical theory behind soliton communication, i.e., the inverse scattering transform (IST), has been exploited to devise a new approach to transmit over single-mode fibers (SMFs). The IST, re-branded as nonlinear Fourier transform (NFT) within the optical communication community, provides a transformation that enables to effectively linearize the nonlinear Schrödinger equation (NLSE) describing the optical wave propagation through a SMF. By using such a transformation, the impact of group velocity dispersion and Kerr nonlinearity can be constructively taken into account to design a novel signaling system that aims at not being limited by signal-signal nonlinear interaction. Furthermore, this transformation may provide more flexible modulation techniques compared to standard coherent approaches, as it associates two spectral quantities to one time-domain waveform: a continuous spectrum corresponding to dispersive waves and a discrete spectrum representing the solitonic solutions [2]. Since the NFT theory strictly requires loss-less, noise-less, and dispersion-slope free transmission, a significant research effort has been devoted into addressing these requirements both numerically, e.g., by using the lossless path-averaged (LPA) approximation [8]–[10], and experimentally, e.g., using distributed Raman amplification [11]–[13]. This has yield several impressive demonstrations by encoding information in either the continuous [14] (up to 3.3 Gb/s over 7344 km), or the discrete spectrum [15] (4 Gb/s over 640 km) [16] (4 Gb/s over 1600 km) [13] (4 Gb/s over 4900 km) and [17] (1.5 Gb/s over 1800 km), finally leading to a recent report of a joint continuous and discrete spectral modulation [18], [19] (up to 64 Gb/s over 976 km). In parallel, the use of SMFs for transmission provides an additional degree of freedom to increase the transmission throughput by exploiting two orthogonal field polarizations. The NFT for the NLSE has therefore been extended

to the Manakov system (MS) [20], where two signal polarizations are transmitted under the assumption that the state-of-polarization varies fast enough to be averaged over the nonlinear and dispersion lengths, and polarization mode dispersion can be neglected. The theory has been applied to numerical and experimental demonstrations of dual-polarization NFT-based transmission using either the continuous [21]–[23] or the discrete spectrum [11], [24]. A dual-polarization transmission where both continuous and discrete spectra are jointly modulated would therefore represent the complete system where all the degrees of freedom for modulation provided by a SMF are exploited.

In this work, we therefore demonstrate joint dual-polarization nonlinear frequency division multiplexing (NFDM) modulation for the first time. First we discuss the framework to perform a joint inverse nonlinear Fourier transform (INFT) operation, i.e., the operation of constructing a dual-polarization time-domain waveform with a desired dual-polarization continuous and discrete spectrum. The steps required are described in details and the numerical algorithms that can be employed to implement the INFT are briefly discussed and numerically characterized. By applying such INFT, a dual-polarization joint NFDM system is experimentally characterized. A transmission distance of up to 3200 km is demonstrated by jointly modulating the dual-polarization signal with a 10-GBd quadrature phase-shift keying (QPSK)-modulated continuous spectrum and a 2-eigenvalue 125-MBd QPSK discrete spectrum, for a total net line rate of 8.4 Gb/s (after forward error correction (FEC) overhead subtraction). The rate is mainly limited by the wide guard intervals required to fulfill the NFT vanishing boundary conditions at the receiver, i.e., after the dispersion-induced signal broadening.

The paper is organized as follows: first in Section II the theoretical framework for joint NFT and INFT operation is provided. The discussion on the transmitter and receiver digital signal processing (DSP) algorithms chosen for implementing the dual-polarization joint NFDM system and the achievable digital back-to-back performance follow in Section III. The experimental setup used as testbed is described in Section IV together with the characterization of the optical back-to-back performance. The transmission results are reported and discussed in Section V and the conclusions drawn in Section VI.

II. Dual-polarization joint continuous and discrete spectral modulation

In this Section, the framework for dual-polarization joint NFDM modulation is described. First the channel model will be briefly outlined in Section II-A, followed by the direct NFT in Section II-B. Finally Section II-C describes in details one of the key contributions of this work, i.e., the joint INFT using the Darboux transform (DT). Throughout this section, bold symbol characters indicate vector or matrices, while their components are indicated with subscripts (without bold): e.g., $\boldsymbol{\phi} = (\phi_1, \ldots, \phi_N)$ and $\mathbf{v} = (v_1, \ldots, v_N)$.

A. Channel model

Let us consider a SMF exhibiting random birefringence, and whose dispersion and nonlinear lengths are much longer than the birefringence correlation length [20]. Under those conditions, the averaged MS describes the evolution in the fiber of the two complex-envelope polarization components of a signal $E_j = E_j(\tau, \ell)$, $j = 1, 2$ [25],

$$\begin{cases} \dfrac{\partial E_1}{\partial \ell} = -j\dfrac{\beta_2}{2}\dfrac{\partial^2 E_1}{\partial \tau^2} + j\dfrac{8\gamma}{9}\left(|E_1|^2 + |E_2|^2\right)E_1 \\ \dfrac{\partial E_2}{\partial \ell} = -j\dfrac{\beta_2}{2}\dfrac{\partial^2 E_2}{\partial \tau^2} + j\dfrac{8\gamma}{9}\left(|E_1|^2 + |E_2|^2\right)E_2 \end{cases} \quad (1)$$

where τ is the retarded time, ℓ the distance, β_2 the group velocity dispersion (GVD), and γ the Kerr nonlinear coefficient of the fiber.

The normalized MS [26] for the anomalous dispersion regime ($\beta_2 < 0$) is

$$\begin{cases} j\dfrac{\partial q_1}{\partial z} = \dfrac{\partial^2 q_1}{\partial t^2} + 2\left(|q_1|^2 + |q_2|^2\right)q_1 \\ j\dfrac{\partial q_2}{\partial z} = \dfrac{\partial^2 q_2}{\partial t^2} + 2\left(|q_1|^2 + |q_2|^2\right)q_2 \end{cases} \quad (2)$$

where t is the normalized retarded time, and z the normalized distance. The equation is derived from (1) through the change of variables

$$q_j(t) = \frac{E_j(\tau)}{\sqrt{P}}, \qquad t = \frac{\tau}{T_0}, \qquad z = -\frac{\ell}{\mathcal{L}}, \qquad (3)$$

with $P = |\beta_2|/(\frac{8}{9}\gamma T_0^2)$, $\mathcal{L} = 2T_0^2/|\beta_2|$, and T_0 is the free normalization parameter.

B. Direct NFT

The direct NFT computes the nonlinear spectrum of the time-domain dual-polarization signal $\mathbf{q}(t) = (q_1(t), q_2(t))$. The spectrum is composed of a continuous (dispersive) part and a finite number of discrete components, which correspond to the solitonic components. The nonlinear spectrum is defined through the Zakharov-Shabat (Z-S) problem [20], [22], [26]

$$\boldsymbol{L}(\mathbf{q})\mathbf{v} = \lambda\mathbf{v} \qquad (4)$$

where $\boldsymbol{L}$ is a 3×3 operator that depends on the signal $\mathbf{q}(t)$, and is given by

$$\boldsymbol{L} = \begin{pmatrix} j\frac{\partial}{\partial t} & -jq_1(t) & -jq_2(t) \\ -jq_1^*(t) & -j\frac{\partial}{\partial t} & 0 \\ -jq_2^*(t) & 0 & -j\frac{\partial}{\partial t} \end{pmatrix}. \qquad (5)$$

The canonical solutions of (4) are the solutions $\boldsymbol{\phi}$, $\bar{\boldsymbol{\phi}}$, $\boldsymbol{\psi}$, and $\bar{\boldsymbol{\psi}}$ defined by the boundary conditions [22], [26]

$$\overbrace{\boldsymbol{\phi}(t, \lambda; \mathbf{q}) \sim \begin{pmatrix} 1 \\ 0 \\ 0 \end{pmatrix}e^{-j\lambda t}, \quad \bar{\boldsymbol{\phi}}(t, \lambda; \mathbf{q}) \sim \begin{pmatrix} 0 & 0 \\ 1 & 0 \\ 0 & 1 \end{pmatrix}e^{j\lambda t}}^{\text{as } t \to -\infty}$$
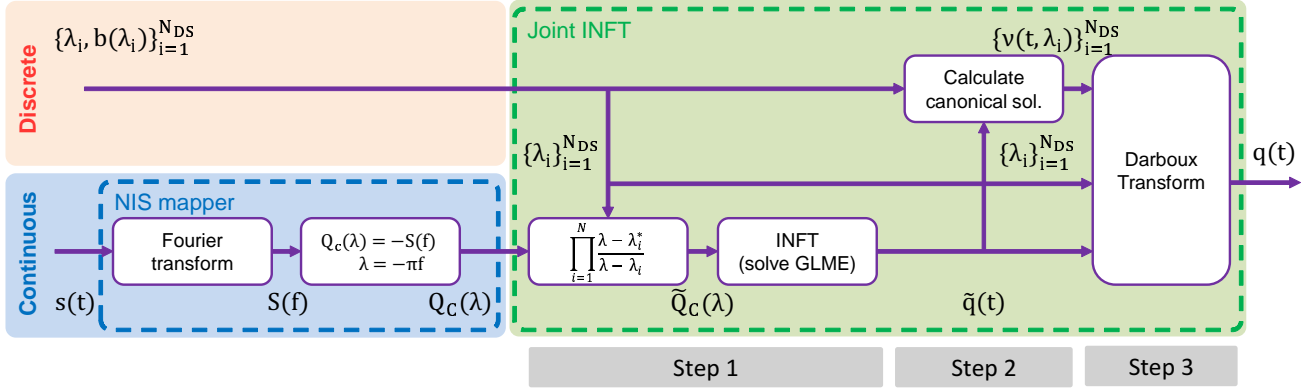
$$(6)$$

Fig. 1. Schematic diagram of dual-polarization joint NFDM time-domain signal generation through a joint INFT operation. The information is first separately encoded into discrete and continuous spectrum, through b-modulation and NIS operation (via the signal Fourier transform $S(f)$), respectively. Then the three steps of the joint INFT follow to obtain the time-domain waveform $q(t)$.

$$\boldsymbol{\psi}(t,\lambda;\mathbf{q}) \sim \begin{pmatrix} 0 & 0 \\ 1 & 0 \\ 0 & 1 \end{pmatrix} e^{j\lambda t}, \quad \bar{\boldsymbol{\psi}}(t,\lambda;\mathbf{q}) \sim \begin{pmatrix} 1 \\ 0 \\ 0 \end{pmatrix} e^{-j\lambda t}$$
$$\underbrace{\qquad\qquad\qquad\qquad\qquad\qquad}_{\text{as } t \to +\infty.}$$
(7)

The canonical solutions form two pairs of bases of the same subspace, consequently there exist some coefficients—known as scattering data—$a(\lambda) \in \mathbb{C}$, and $\mathbf{b}(\lambda) \in \mathbb{C}^{2\times 1}$ such that

$$\boldsymbol{\phi}(t,\lambda) = \boldsymbol{\psi}(t,\lambda)\mathbf{b}(\lambda) + \bar{\boldsymbol{\psi}}(t,\lambda)a(\lambda). \quad (8)$$

Such scattering data can be obtained as

$$a(\lambda) = \lim_{t \to +\infty} \phi_1(t,\lambda)e^{+j\lambda t}, \quad (9a)$$

$$b_1(\lambda) = \lim_{t \to +\infty} \phi_2(t,\lambda)e^{-j\lambda t}, \quad (9b)$$

$$b_2(\lambda) = \lim_{t \to +\infty} \phi_3(t,\lambda)e^{-j\lambda t}, \quad (9c)$$

and are related to each other by

$$|a(\lambda)|^2 + |b_1(\lambda)|^2 + |b_2(\lambda)|^2 = 1. \quad (10)$$

The continuous spectrum of the time domain signal $\mathbf{q}(t)$ is defined as

$$\mathbf{Q_c}(\lambda) = \mathbf{b}(\lambda)/a(\lambda), \quad \lambda \in \mathbb{R}. \quad (11)$$

The discrete spectrum is made of a finite number N_{DS} of eigenvalues $\lambda_i \in \mathbb{C}^+$ such that $a(\lambda_i) = 0$. Each eigenvalue has an associated spectral amplitude (also referred to as norming constant) defined as

$$\mathbf{Q_d}(\lambda_i) = \mathbf{b}(\lambda_i)/a'(\lambda_i), \quad \lambda_i \in \mathbb{C}^+. \quad (12)$$

with $a'(\lambda_i) = \frac{da(\lambda)}{d\lambda}|_{\lambda=\lambda_i}$.

Several methods to perform the NFT numerically are available for the single polarization scenario [2], [3], [27] and for the dual polarization case [21], [22], [24]. In this work, the trapezoidal discretization method was used for computing both the continuous and the discrete spectrum [28].

C. Inverse NFT

The INFT is the operation to generate a time domain signal from a given nonlinear spectrum. Several methods exist to numerically perform the INFT for the scalar (single polarization) NLSE [2], [3], [9], [18], [29]. Additionally, the theory can be extended to the MS [26] and a few techniques reported leading to recent numerical analysis and experimental demonstrations: the DT for the MS [24] for a multi-soliton signal (no continuous spectrum), the inverse Ablowitz-Ladik method for a signal with only continuous spectrum [21], and the Nyström conjugate gradient (NCG) method—based on the solution of the Gelfand-Levitan-Marchenko equation (GLME)—that can be applied to a full spectrum [22], [30]. However, when the overall energy of the signal, and so of the nonlinear spectrum, is too high, the latter method may diverge [22]. This issue becomes relevant in optical communication when discrete eigenvalues are used for modulation [22]. In this section, we describe an alternative method to generate a time domain signal from a given continuous and discrete nonlinear spectrum. Extending the concepts of [18], [28] to the MS, the method uses an INFT algorithm (e.g., the NCG in this work) to obtain the time-domain signal corresponding to a pre-modified continuous spectrum, and then adds the discrete eigenvalues using the DT [24], [31]. Using this approach, the aforementioned issues of NCG can be relaxed as the energy of the input to the NCG is decreased by the large amount carried by the discrete spectrum, therefore shifting the energy barrier to higher energy levels. A choice of initialization parameters is further provided to ensure that the obtained signal has the desired nonlinear spectrum, by following the approach in [24], [28]. Whereas the algorithm for single polarization in [18] is supported by the mathematical framework demonstrated in [28], a rigorous mathematical framework is beyond the scope of this work. The numerical accuracy of the scheme is rather confirmed a posteriori with numerical simulations (see Section III) and relies on following the single-polarization framework of [18], [28] similarly to the approach of [24]. Similarly to the single-

polarization case, the three steps are illustrated below.

Assume that we want to digitally compute the time domain signal $\mathbf{q}(t)$ corresponding to the continuous spectrum $\mathbf{Q_c}(\lambda)$ and the discrete spectrum $\{\lambda_i, \mathbf{b}(\lambda_i)\}_{i=1}^{N_{DS}}$, adopting $\mathbf{b}$-modulation on the discrete part as will be discussed in Section III. The choice of b-modulation is not a strict requirement for the scheme presented in the following, and the approach can be easily extended to mapping techniques other than b-modulation.

The algorithm consists of three steps (illustrated in Fig. 1):

1) Use the INFT to compute the time domain signal $\widetilde{\mathbf{q}}(t)$ corresponding to the pre-modified continuous spectrum

$$\widetilde{\mathbf{Q}}_{\mathbf{c}}(\lambda) = \mathbf{Q_c}(\lambda) \prod_{i=1}^{N_{DS}} \frac{\lambda - \lambda_i}{\lambda - \lambda_i^*} \qquad (13)$$

and with empty discrete spectrum. This can be achieved by solving the GLME equation, for example using the NCG method. [22].

2) For each eigenvalue λ_i for $i = 1, \ldots, N_{DS}$, obtain the solution $\boldsymbol{\nu}(t, \lambda_i)$ of the eigenvalue problem $\boldsymbol{L}(\widetilde{\mathbf{q}})\mathbf{v} = \lambda_i \mathbf{v}$ with boundary conditions

$$\begin{cases} \nu_1(T, \lambda_i) = 1 \\ \nu_2(-T, \lambda_i) = -b_1(\lambda_i) \\ \nu_3(-T, \lambda_i) = -b_2(\lambda_i) \end{cases} \qquad (14)$$

where $\widetilde{\mathbf{q}}(t) = 0$ for $t \notin [-T, T]$. The solution $\boldsymbol{\nu}(t, \lambda_i)$ can be obtained as

$$\boldsymbol{\nu}(t, \lambda_i) = \frac{\boldsymbol{\phi}(t, \lambda_i)}{\phi_1(T, \lambda_i)} - \boldsymbol{\psi}(t, \lambda_i)\boldsymbol{\psi}^{(2)}(-T, \lambda_i)^{-1}\mathbf{b}(\lambda_i), \qquad (15)$$

where $\boldsymbol{\phi}(t, \lambda_i)$ and $\boldsymbol{\psi}(t, \lambda_i)$ are the canonical solutions of $\boldsymbol{L}(\widetilde{\mathbf{q}})\mathbf{v} = \lambda_i \mathbf{v}$ (see Section II-B) and $\boldsymbol{\psi}^{(2)}(t, \lambda_i)$ is the 2×2 matrix made of the second and the third rows of $\boldsymbol{\psi}(t, \lambda_i)$, i.e.,

$$\boldsymbol{\psi}^{(2)}(t, \lambda_i) = \begin{pmatrix} \psi_{21} & \psi_{22} \\ \psi_{31} & \psi_{32} \end{pmatrix}. \qquad (16)$$

Note that Eq. (15) is a solution of the eigenvalue problem because it is a linear combination of solutions. Furthermore, it verifies the boundary conditions Eq. (14). The canonical solutions $\boldsymbol{\phi}(t, \lambda_i)$ and $\boldsymbol{\psi}(t, \lambda_i)$ can be found with standard methods used for the NFT (see Section II-B). Additionally, if modulation techniques other than b-modulation are chosen, a different mapping can be easily derived starting from Eq. (15).

3) Execute the DT for the MS, as in [24], [31], with input parameters $\widetilde{\mathbf{q}}(t)$, $\{\lambda_i\}_{i=1}^{N_{DS}}$, and $\{\boldsymbol{\nu}(t, \lambda_i)\}_{i=1}^{N_{DS}}$ to iteratively add the discrete spectrum $\{\lambda_i, \mathbf{b}(\lambda_i)\}_{i=1}^{N_{DS}}$ to the spectrum of $\widetilde{\mathbf{q}}(t)$. The $\boldsymbol{\nu}(t, \lambda_i)$ are the generic auxiliary solutions. The solution $\mathbf{q}(t)$ obtained in this manner has continuous spectrum $\mathbf{Q_c}(\lambda)$ and discrete spectrum $\{\lambda_i, \mathbf{b}(\lambda_i)\}_{i=1}^{N_{DS}}$.

This scheme can be easily verified numerically by computing the direct NFT of the generated time-domain signal and comparing the resulting spectra with the desired ones.
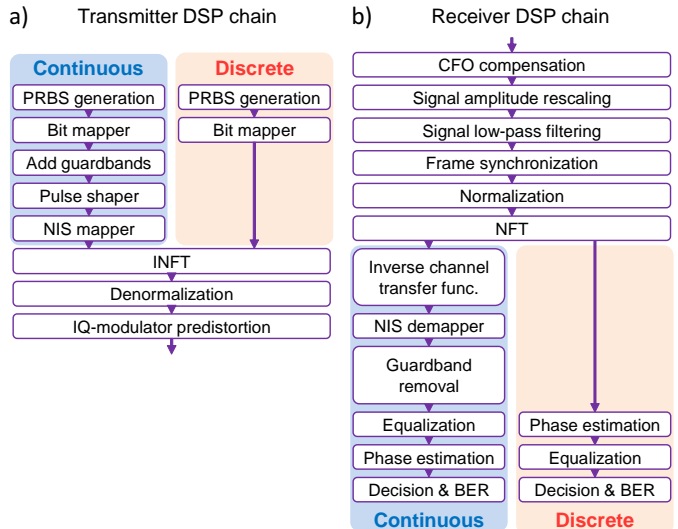

Fig. 2. (a) Transmitter and (b) receiver digital signal processing chains, highlighting the key operations performed on the digital waveforms.

III. Digital signal processing

The DSP chains implemented at the transmitter and receiver to properly encode the data into a digital waveform (transmitter) and extract it back (receiver) are shown in Fig. 2 (a) and (b), respectively.

A pseudo-random bit sequence is generated at the transmitter side to be encoded in both the continuous and discrete spectra. For the continuous spectrum, after mapping the bits into 10-GBd QPSK symbols (16 samples/symbol), guard intervals of 64 symbols are added for each 16-symbol burst, leading to an overall NFDM symbol (burst) length of 8 ns. Such guard intervals ensure that no inter-burst interference takes place after the dispersion-induced pulse broadening at the maximum transmission distance considered in this work, i.e., 3200 km. Such long guard intervals could be decreased by adding dispersion pre-compensation at the transmitter side. This was avoided for the experimental investigation since dispersion pre-compensation would yield digital waveforms with different peak-to-average power ratio (PAPR) for each transmission distance, making it more challenging to compare performance at different distances. The symbols are pulse-shaped with a raised cosine filter (roll-off of 1) and the NIS is used to obtain the continuous spectrum as detailed in Fig. 1: the Fourier transform of the pulse-shaped time-domain signal is directly mapped into the continuous spectrum $\mathbf{Q_c}(\lambda)$ [10].

The data bits to be encoded onto the discrete spectrum are also mapped to QPSK symbols. Then, the symbols are associated to the $\mathbf{b}(\lambda_i)$ (b-modulation) corresponding to the two purely-imaginary eigenvalues, $\lambda_i \in \{0.3j, 0.6j\}$ that have been chosen. The free time normalization parameter defined in (3) is chosen to be $T_0 = 244$ ps. The eigenvalues themselves are not modulated, i.e., in each symbol-slot, both eigenvalues are transmitted. Additionally, several recent works clearly showed that modulating directly

the $\mathbf{b}(\lambda_i)$ (**b**-modulation) of the discrete spectrum leads to a lower correlation and thus better performance than modulating $\mathbf{Q_d}(\lambda_i)$ ($\mathbf{Q_d}(\lambda)$-modulation). In this work we therefore focus on **b**-modulation for the discrete spectrum [12], [32]. The radii of the two QPSK constellations have been set to $5\sqrt{2}$ and $0.05\sqrt{2}$, for the $\mathbf{b}(\lambda_i)$ associated to λ_1 and λ_2, respectively. This choice leads to a temporal separation of the components of the time-domain signal associated to the NFT coefficients $\mathbf{b}(\lambda_i)$ corresponding to different eigenvalues. The separation is such that the discrete spectral components (at the transmitter output) are placed in time within the guard intervals of the continuous-spectrum burst. The one corresponding to $\mathbf{b}(\lambda_1)$ can be seen in Fig. 3(a) after the burst encoded in the continuous spectrum, whereas the waveform corresponding to $\mathbf{b}(\lambda_2)$ is located on the opposite end of the symbol slot. This choice was made to avoid additional signal-dependent implementation penalties due to high PAPR at the transmitter side, as well as to limit the time-frequency product of the multi-soliton signal [33]. Nevertheless, continuous and discrete time-components do interact during fiber propagation. An INFT operation is then performed as described in Section II-C to generate a time-domain waveform with the desired continuous and discrete spectra. After proper denormalization, the waveform shown in Fig. 3(a) is obtained (signal power of -9.2 dBm with the fiber parameters of Section IV). The figure clearly shows the two discrete (solitonic) components with the continuous (dispersive) components in between. Finally, the waveforms are pre-distorted to account for the nonlinear transfer function of the IQ modulator by applying an $\arcsin(\cdot)$ function. Such a digital waveform can then be encoded onto an optical carrier using a standard IQ modulator, after digital-to-analog conversion, as will be described in Section IV. The net line rate of the generated signal is 8.4 Gb/s, taking into account the 80%-guard intervals applied and the 7%-hard-decision forward error correction (HD-FEC) overhead [34], [35].

At the receiver side, the digital waveforms are then processed by the DSP highlighted in Fig 2(b). First, carrier frequency offset (CFO) compensation is performed to remove any frequency shift due to frequency mistmatch between signal and local oscillator (LO), followed by signal amplitude rescaling, low-pass filtering at twice the 20-dB signal bandwidth, and frame synchronization. The direct NFT described in Section II-B is then applied to recover the continuous and discrete spectra from the time-domain waveform. The inverse transfer function of the channel $\exp\left(4j\lambda^2 z\right)$ is first applied to the continuous part of the spectrum, followed by NIS demapping with the opposite transformation applied at the transmitter side: first $\mathbf{Q_c}(\lambda)$ is mapped into the Fourier spectrum, then a inverse Fourier transform is used to recover the time-domain waveform [10]. The guard intervals are subsequently removed and blind radius-directed equalization is performed followed by phase estimation using digital phase-lock loop. Finally, decisions on the symbols are taken and the bit error rate (BER) is counted. The

steps for the demodulation of the discrete spectrum consists of first phase recovery using blind phase search (BPS) independently on each constellation $b_j(\lambda_i)$, followed by NFT-domain equalization [11], [12]. As the chosen eigenvalues are purely imaginary, BPS inherently applies the ideal inverse channel transfer function, which consists of a constant phase rotation. After BPS, NFT-domain equalization reduces the noise on the $b_j(\lambda_i)$ by exploiting the correlation between the received eigenvalues and the spectral amplitudes [11], [12]. This equalizer enables to partially compensate for the rotation and re-scaling experienced by $b_1(\lambda_i)$ and $b_2(\lambda_i)$ due to the displacement of the eigenvalues. After equalization, decisions are taken and BER counting is performed.

The DSP chains and numerical algorithm have been first benchmarked in a digital back-to-back scenario where the digital waveforms before the IQ-modulator predistortion are fed directly into the receiver DSP chain. This analysis allows to ignore the impact of practical equipment limitations, such as analog-to-digital converter (ADC) and digital-to-analog converter (DAC) resolution, and electrical/optical noise sources, to focus on the numerical algorithms. The resulting performance is shown in Fig. 3(b), as a function of the energy in the continuous spectrum, comparing joint and continuous-only modulation. For the joint modulation (top figure in Fig. 3(b)), the energy in the discrete spectrum is kept constant to fulfill the duration-amplitude relation [2]. The signal quality is evaluated by calculating the error vector magnitude (EVM) as the BER values are too low for reliable error counting [36].

In the case of joint modulation, as the energy in the continuous spectrum increases, the performance of the continuous spectrum improves (EVM decreases) with an optimum at approx. 0.18 pJ (-9.2 dBm of launch power). When the energy in the continuous spectrum approaches zero, the discrete spectrum is dominant and worsens the accuracy of the numerical algorithms for the continuous part. In the case of continuous-only modulation (bottom figure in Fig. 3(b)), the performance do not degrade as the energy decreases as for the joint-modulation, thus ruling out numerical errors of the NCG alone.

Beyond the optimum energy for the joint-modulation, the performance worsens rather rapidly above -9.0 dBm. A similar worsening of the performance is indeed reflected when no discrete spectrum is present. Note that, considering **b**-modulation also for the continuous spectrum (instead of modulating directly $\mathbf{Q_c}(\lambda)$) may provide further improvement [27] even though using it in the context of joint spectral modulation may present some challenges [37]. Fig. 3(b) shows also the impact of the energy in the continuous spectrum on the quality of the discrete spectrum. As the energy in the continuous spectrum is increased, the limited precision of the numerical algorithms yields a loss of orthogonality between continuous and discrete spectrum, thus decreasing the performance of the latter when the continuous components at high energy overlap with the solitons. The impact of the
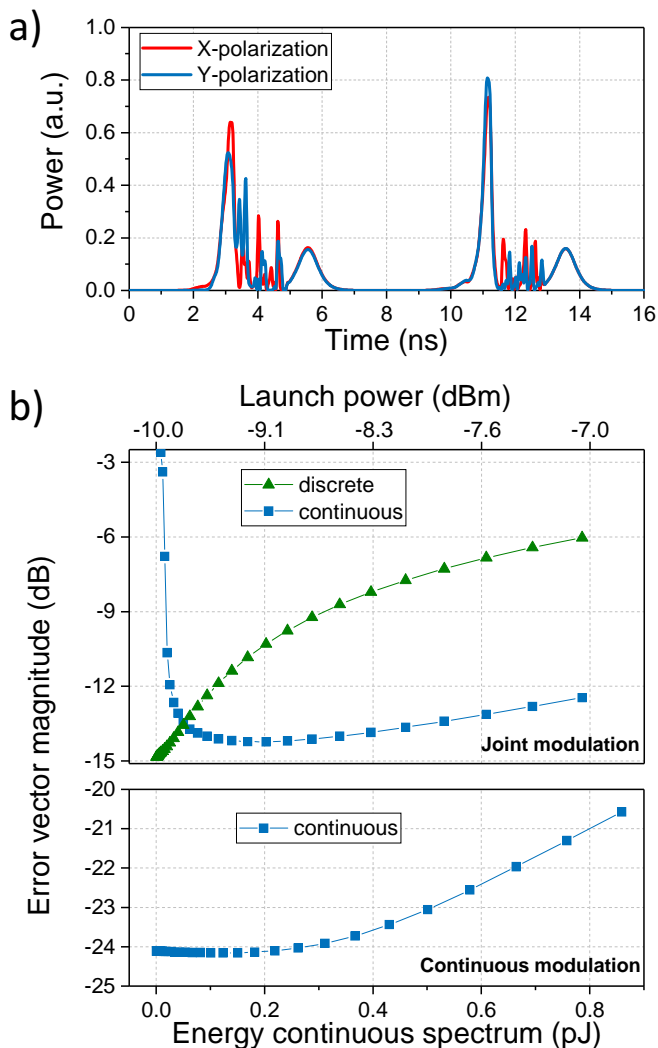
Fig. 3.   (a) Time-domain waveforms (-9.2-dBm launch power, 2 NFDM symbols, X and Y polarizations) showing the discrete (solitonic) components with the continuous components in between and (b) digital back-to-back performance: EVM as a function of the energy in the continuous spectrum for joint modulation (top) and continuous-only modulation (bottom).

time-overlap is expected to worsen the performance during transmission over a non-ideal (lossy and noisy) channel, as discussed in [38]. Furthermore, the numerical precision of the INFT is also expected to contribute to the overall worsening of the performance of the discrete spectrum.

Regardless of these limitations and the consequent energy balance between continuous and discrete spectrum, the BER that can be estimated from the EVM is well below 1×10^{-4}, even for the highest power values considered.

IV. Experimental transmission setup

The experimental setup is shown in Fig. 4. The pre-distorted digital waveforms generated as in Fig. 2(a) are loaded into a 4-channel 64-GSamples/s arbitrary waveform generator (AWG) driving the IQ modulator, which encodes the dual-polarization NFDM signal into an optical carrier generated by a low-linewidth (≤ 1 kHz) fiber laser. The same laser is used as LO at the receiver side.

The transmission link consists of a recirculating transmission loop based on four 50-km transmission spans with distributed Raman amplification applied to each span as in [11]. Backward pumping combined with low-loss large effective area fiber (SCUBA fiber) enables to achieve maximum power variations of approximately 3 dB across the full 200-km loop length. The power profile measured by optical time domain reflectometry is shown in inset (a) of Fig. 4. Loss, dispersion, and nonlinear coefficient of the transmission fiber are 0.155 dB/km, 22 ps/nm/km, and 0.6 /W/km, respectively. These values have been used for the (I)NFT (de)normalization as discussed in Section II-A. In addiction to the transmission fiber, the loop consists of acusto-optic modulators (AOMs) used as optical switches, an optical band pass filter (OBPF) (0.5-nm bandwidth) which suppresses out-of-band amplified spontaneous emission (ASE) noise, an isolator (ISO), and an erbium-doped fiber amplifier (EDFA) which compensates for the power loss of all these components.

After the chosen number of recirculation turns, the signal is received with a pre-amplified coherent receiver using four balanced photodetectors (BPDs) and a 80-GSamples/s digital storage oscilloscope (DSO) acting as analog-to-digital converter. For simplicity, the signal polarization is manually aligned at the receiver input with a polarization controller (PC). However, demultiplexing schemes based on training sequences have already been reported [23]. After analog-to-digital conversion, the waveforms are processed offline by the DSP discussed in Section III and the performance are evaluated by bit error counting performed on more than 10^6 bits, ensuring a reliable BER above 10^{-5}. Only BER values from direct error counting are reported for experimental measurements. In the following the transmission reach is evaluated considering the HD-FEC threshold (BER of 3.8×10^{-3}) [34], [35]. Remark that the frequency-offset estimation discussed in Section III is necessary due to the frequency shift introduced by the AOMs which results in self-heterodyne detection rather than homodyne. An example of constellation diagrams for continuous and discrete spectrum is shown in inset (b) of Fig. 4 after 2800-km transmission, illustrating the high quality of the received signals.

Before discussing the transmission results in Section V, the signal performance are evaluated in back-to-back configuration, i.e., connecting the receiver directly at the output of the IQ modulator. The results are shown in Fig. 5, distinguishing between the performance of continuous and discrete spectral components as well as showing the total BER. The optical signal-to-noise ratio (OSNR) at the output of the transmitter was approx. 33.8 dB for all the launch powers considered.

For these back-to-back results, the total BER is dominated by the BER of the continuous spectrum as more bits are encoded in the continuous spectrum (64 bits/NFDM symbol) compared to the discrete spectrum (8 bits/NFDM
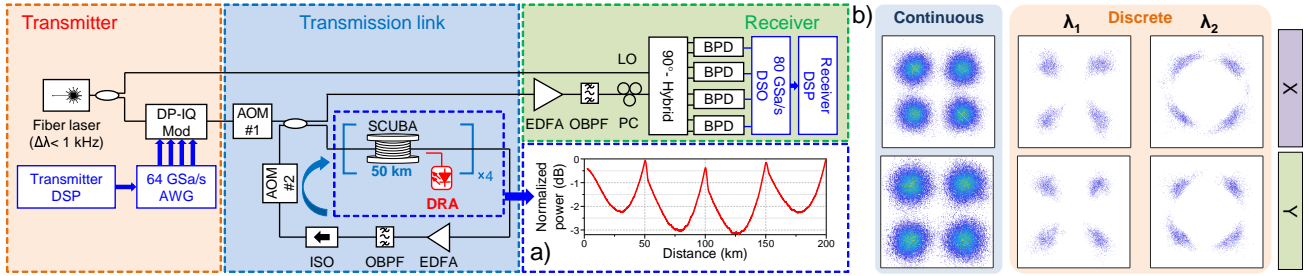
Fig. 4. Experimental setup for the transmission of the jointly modulated signal in a recirculating transmission loop. Insets: (a) power profile measured over a loop recirculation and (b) constellation diagrams after 2800-km transmission.
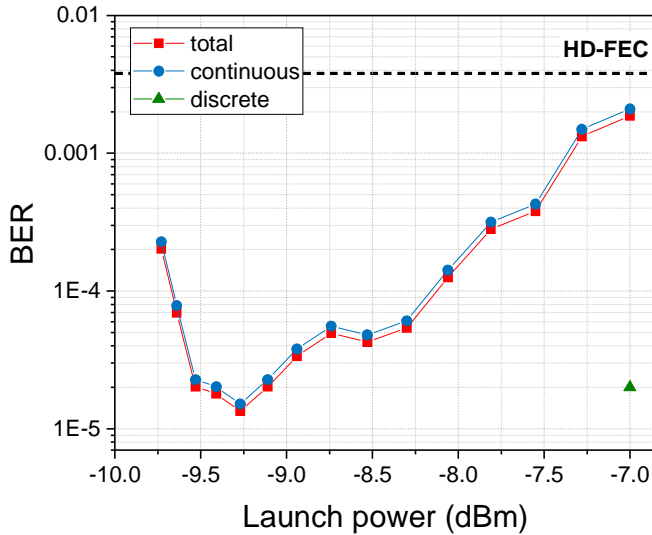

Fig. 5. Optical back-to-back BER performance from direct error counting as a function of the launch signal power.
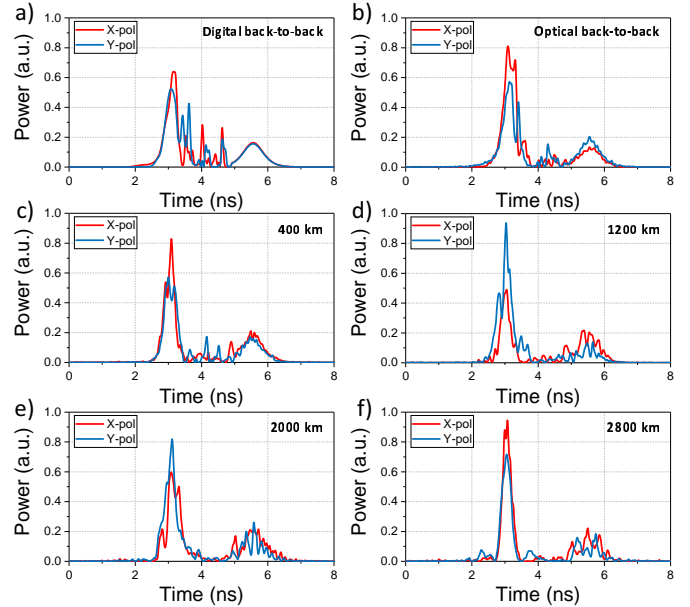

Fig. 6. Examples of time-domain waveforms showing one 8-ns NFDM symbols (including guard intervals) at a fixed launch power of -9.2 dBm: (a) digital back-to-back, (b) optical back-to-back and after (c) 400-km, (d) 1200-km, (e) 2000-km, (f) and 2800-km transmission. The bit patter is not the same for the same for the different waveforms.

symbol). Therefore, a higher error probability can be tolerated on the discrete spectrum before it starts affecting the total BER. As discussed for the numerical results of Fig. 3, the BER of the continuous spectrum improves with its increased energy, reaches an optimum and worsens due to numerical instabilities. Note that the optimum power is the same for the digital back-to-back (see Fig. 3(b)). The lack of variations in the optimum power hints that the dominant limitation is currently related to the numerical algorithms, whereas the impact of electrical/optical noise at transmitter and receiver, as well as the AWG resolution are rather negligible. The BER on the discrete spectrum is also consistent with Fig. 3(b), as errors are only detected at the highest launch power considered, -7 dBm. At such a power level, the estimated BER in digital back-to-back was estimated to almost the same value, showing that a negligible penalty is introduced by the optical-frontends (at both transmitter and receiver) also for the discrete spectrum.

V. Transmission performance

After having evaluated the system performance for both digital and optical back-to-back, the transmission performance is reported in this section. Fig. 6 shows the evolution along the fiber of one NFDM symbol at the optimum launch power of -9.2 dBm. The waveforms clearly show the interaction in time between the discrete and continuous spectral components, whereas the guard interval size is more than sufficient to guarantee the vanishing boundary conditions required by the NFT also at the longest transmission distances. The guard interval size could actually be reduced by pre-dispersing the waveforms at the transmitter side by half of the transmission length, i.e., by applying the inverse of the channel transfer function [39]. Additionally, by tailoring the guard intervals to the desired transmission distance, the transmission rate can be maximized. The total BER results as a function of the launch power for different transmission distances are shown in Fig. 7(a). The curves show an optimum launch power (minimum BER) consistent with the digital and optical back-to-back performance, i.e., −9.2 dBm. The BER values after a 400-km transmission are actually
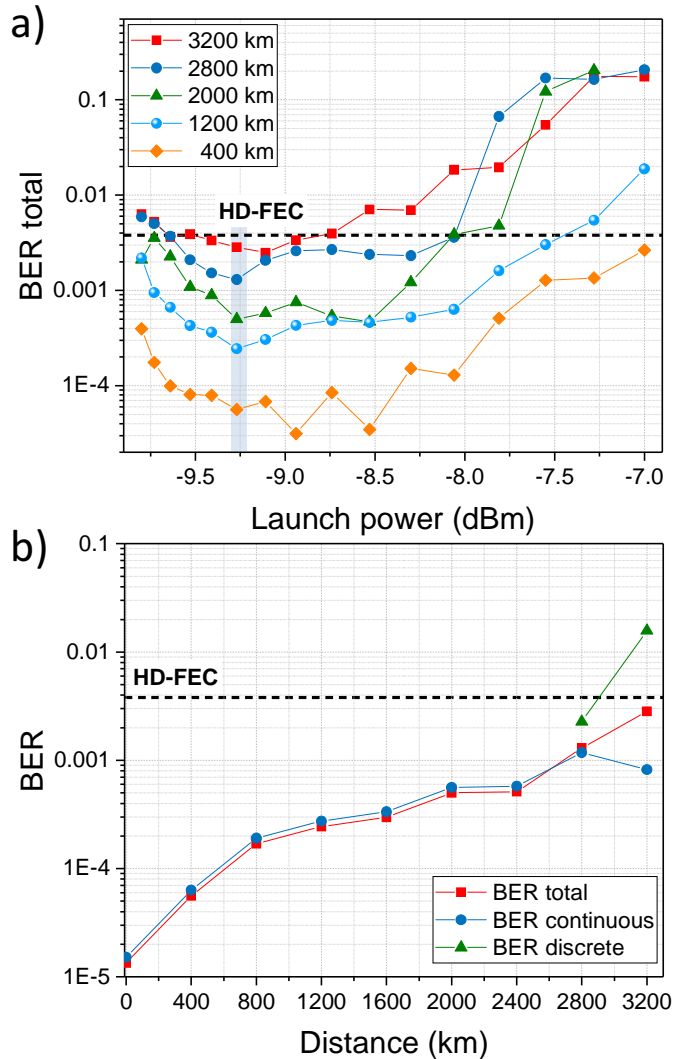
Fig. 7. (a) Total BER performance as a function of the launch power for different transmission distances, and (b) total BER and contributions from continuous and discrete spectrum as a function of the transmission distance for the optimum launch power of -9.2 dBm (shaded area in (a)).

in close agreement with the optical back-to-back ones in Figs. 3(b). These results further confirm that the dominant performance limitation is currently linked to the numerical precision in performing joint INFT and NFT at high power values. By increasing the numerical precision of the different steps (Section II) using improved numerical algorithms, we believe the performance could be significantly improved, potentially shifting the optimum launch power to higher values [40].

The BER as a function of the transmission distance is shown in Fig. 7(b), for a fixed -9.2-dBm launch power. The figure highlights that BER below the HD-FEC threshold can be achieved for up to 3200-km transmission. Beyond 2800 km, the dominant contribution to the total BER comes from the discrete spectral components and in particular from the largest eigenvalue $\lambda_2 = 0.6j$. Improved modulation schemes for the discrete spectral components, such as the differential modulation proposed in [41] or

soliton detection based on matched filter [18], are thus expected to increase the transmission reach. Furthermore, as far as the continuous spectrum is concerned using improved detection strategies, may also provide additional performance gain [42], [43]. Finally, the net transmission rate may be increased by reducing the guard intervals, as mentioned above, and pre-dispersing the signal by half of the transmission length at the transmitter side [19], [39], [44].

VI. Conclusion

We have introduced a framework for dual-polarization NFDM systems which allows encoding data on both continuous and discrete spectral components. The steps to perform the joint INFT at the transmitter side are described and numerically implemented, evaluating its performance first in a transmission-free scenario without (digital back-to-back) and with the optical front-ends (optical back-to-back) considered. The dual-polarization joint NFDM system has then been experimentally demonstrated in a transmission scenario using distributed Raman amplification. A transmission reach of 3200 km is achieved for a 8.4-Gb/s net rate NFDM signal, mainly limited by the numerical implementation of the joint INFT and NFT, which will need to be further improved. This work demonstrates the use of all the degrees of freedom available for NFDM-based transmission over SMFs.

Acknowledgment

References

[1] A.D. Ellis, M.E. McCarthy, M.A.Z. Al Khateeb, M. Sorokina, and N.J. Doran, "Performance limits in optical communications due to fiber nonlinearity," Advances in Optics and Photonics 9(3), 429–503 (2017).
[2] M. Yousefi, and F.R. Kschischang, "Information transmission using the nonlinear Fourier transform, Part I-II-III," IEEE Transactions on Information Theory 60(7), 4312–4369 (2014).
[3] S.K. Turitsyn, J.E. Prilepsky, S.T. Le, S. Wahls, L.L. Frumin, M. Kamalian, and S.A. Derevyanko, "Nonlinear Fourier transform for optical data processing and transmission: advances and perspectives," Optica 4(3), 307–322 (2017).
[4] A. Hasegawa and F. Tappert, "Transmission of stationary non-linear optical pulses in dispersive dielectric fibers. I. Anomalous dispersion," Applied Physics Letters 23(3), 142–144 (1973).
[5] L. Mollenauer and K. Smith, "Demonstration of soliton transmission over more than 4000 km in fiber with loss periodically compensated by Raman gain," Optics letters 13(8), 675–677 (1988).
[6] M. Nakazawa, E. Yamada, H. Kubota, and K. Suzuki, "10 Gbit/s soliton data transmission over one million kilometres," Electronics Letters 27(14), 1270–1272 (1991).
[7] A. Hasegawa, and T. Nyu, "Eigenvalue communication," Journal of Lightwave Technology 11(3), 395–399, Mar 1993.
[8] S.K. Turitsyn, B.G. Bale, and M.P. Fedoruk, "Dispersion-managed solitons in fibre systems and lasers," Physics Reports 521(4), 135–203 (2012).

[9] S.T. Le, J.E. Prilepsky, P. Rosa, J.D. Ania-Castañón and S.K. Turitsyn, "Nonlinear inverse synthesis for optical links with distributed Raman amplification," Journal of Lightwave Technology 34(8), 1778–1786 April 2016.

[10] S.T. Le, J.E. Prilepsky, and S.K. Turitsyn, "Nonlinear inverse synthesis technique for optical links with lumped amplification," Optics Express 23(7) 8317–8328 (2015).

[11] S. Gaiairin, F. Da Ros, N. De Renzis, E.P. da Silva, and D. Zibar, "Dual-polarization NFDM transmission using distributed Raman amplification and NFT-domain equalization," IEEE Photonics Technology Letters, accepted for publication.

[12] T. Gui, T.H. Chan, C. Lu, A.P.T. Lau, and P.-K.A. Wai, "Alternative decoding methods for optical communications based on nonlinear Fourier transform," Journal of Lightwave Technology 35(9), 1542-1550 May 2017.

[13] A. Gejsler, J. Leibrich, C.G. Schäffer, "Influence of non-ideal first order counter-propagating raman amplification on discrete nonlinear Fourier spectrum based communication," in Proc. Photonic Networks; 19th ITG-Symposium (2018).

[14] S.T. Le, I.D. Philips, J.E. Prilepsky, P. Harper, A.D. Ellis, and S.K. Turitsyn, "Demonstration of nonlinear inverse synthesis transmission over transoceanic distances," Journal of Lightwave Technology 34(10), 2459–2466, May 2016.

[15] V. Aref, H. Bülow, K. Schuh, and W. Idler, "Experimental demonstration of nonlinear frequency division multiplexed transmission," in Proc. ECOC 2015, paper 0372.

[16] H. Bülow, V. Aref, K. Schuh, and W. Idler, "Experimental Nonlinear Frequency Domain Equalization of QPSK Modulated 2-Eigenvalue Soliton," in Proc. OFC 2016, paper Tu2A.3.

[17] Z. Dong, S. Hari, T. Gui, K. Zhong, M.I. Yousefi, C. Lu, P.-K.A. Wai, F.R. Kschischang, and A.P.T. Lau "Nonlinear frequency division multiplexed transmissions based on NFT," IEEE Photonics Technology Letters 27(15), 1621–1623 (2015).

[18] V. Aref, S.T. Le, and H. Bülow, "Modulation Over Nonlinear Fourier Spectrum: Continuous and Discrete Spectrum," Journal of Lightwave Technology 36(6), 1289–1295, March 2018.

[19] S.T. Le, V. Aref, and H. Bülow, "Nonlinear signal multiplexing for communication beyond the Kerr nonlinearity limit," Nature Photonics 11, 570-576 (2017).

[20] S.V. Manakov, "On the theory of two-dimensional stationary self-focusing of electromagnetic waves," Soviet Physics-JETP 38(2), 248-253 (1974).

[21] J.-W. Goossens, M.I. Yousefi, Y. Jaouën, and H. Hafermann, "Polarization-division multiplexing based on the nonlinear Fourier transform," Optics Express 25(22), 26437-26452 (2017).

[22] S. Civelli, S.K. Turitsyn, M. Secondini, and J.E. Prilepsky, "Polarization-multiplexed nonlinear inverse synthesis with standard and reduced-complexity NFT processing," Optics Express 26(13), 17360-17377 (2018).

[23] T. Gui, W.A. Gemechu, J.-W. Goossens, M. Song, S. Wabnitz, M.I. Yousefi, H. Hafermann, A.P.T. Lau, and Y. Jaouën, "Polarization-division-multiplexed nonlinear frequency division multiplexing," in Proc. CLEO 2018, paper STu4C.3.

[24] S. Gaiarin, A.M. Perego, E.P. da Silva, F. Da Ros, and D. Zibar, "Dual-polarization nonlinear Fourier transform-based optical communication system" Optica 5(3), 263-270 (2017).

[25] C.R. Menyuk, and B.S. Marks, "Interaction of polarization mode dispersion and nonlinearity in optical fiber transmission systems," Journal of Lightwave Technology 24(7), 2806–2826 July 2006.

[26] M. J. Ablowitz, B. Prinari, and A.D. Trubatch, "Discrete and continuous nonlinear Schrdinger systems," Cambridge University Press (2004).

[27] S. Wahls, "Generation of time-limited signals in the nonlinear Fourier domain via b-modulation," in Proc. ECOC 2017, paper W.3.C.6.

[28] V. Aref, " Control and Detection of Discrete Spectral Amplitudes in Nonlinear Fourier Spectrum," arXiv:1605.06328.

[29] S. Civeli, L. Barletti, and M. Secondini, "Numerical methods for the inverse nonlinear Fourier transform," in Proc. TIWDC 2015, 13–16 (2015).

[30] A. Aricó, G. Rodriguez, and S. Seatzu, "Numerical solution of the nonlinear Schrdinger equation, starting from the scattering data," Calcolo, 48(1), 75–88, March 2011.

[31] O.C. Wright, "The Darboux transformation of some Manakov systems," Applied Mathematics Letters 16(5), 647–652 (2003).

[32] H. Bülow, V. Aref, and L. Schmalen, "Modulation on discrete nonlinear spectrum: perturbation sensitivity and achievable rates," IEEE Photonics Technology Letters, 30(5), 423–426 (2018).

[33] A. Span, V. Aref, H. Bülow, and S. ten Brink, "On time-bandwidth product of multi-soliton pulses," arXiv:1705.09468v1 (2017).

[34] E. Agrell, and M. Secondini, "Information-theoretic tools for optical communications engineers," in Proc. IPC 2018, paper MA3.1.

[35] H. Sun, K. Wu, and K. Roberts, "Real-time measurements of a 40 Gb/s coherent system," Optics Express 16(2), 873879 (2008).

[36] R.A. Shafik, M.S. Rahman, and A.R. Islam, "On the extended relationships among EVM, BER and SNR as performance metrics," in Proc. ICECE 2006, pp. 408411.

[37] T. Gui, G. Zhou, C. Lu, A.P.T. Lau, and S. Wahls, "Nonlinear frequency division multiplexing with b-modulation: shifting the energy barrier," Optics Express 26(12), 27978–27990 (2018).

[38] V. Aref, S.T. Le, and H. Bülow "Does the cross-talk between nonlinear modes limit the performance of NFDM systems?," in Proc. ECOC 2017, paper Th.1.D.1.

[39] I. Tavakkolnia, and M. Safari, "Dispersion pre-compensation for NFT-based optical fiber communication systems," in Proc. CLEO 2016, paper SM4F.4.

[40] S. Chimmalgi, P.J. Prins, and S. Wahls, "Fast nonlinear Fourier transform algorithms using high order exponential integrators," arXiv:1812.00703v1 (2018).

[41] A. Span, V. Aref, H. Bülow, and S. ten Brink, "Precoding for dual polarization soliton transmission," in Proc. OECC 2018, paper 4B3-3.

[42] S. Civelli, E. Forestieri, and M. Secondini, "Decision-feedback detection strategy for nonlinear frequency-division multiplexing," Optics Express 26(9), 12057–12071 (2018).

[43] R.T. Jones, S. Gaiarin, M.P. Yankov, and D. Zibar, "Time-domain neural network receiver for nonlinear frequency division multiplexed systems,", IEEE Photonics Technology Letters 30(12), 1079–1082 (2018).

[44] S. Civelli, E. Forestieri, and M. Secondini, "Why noise and dispersion may seriously hamper nonlinear frequency-division multiplexing," IEEE Photonics Technology Letters 29(16), 1332–1335 (2017).